RSC Advances

ROYAL SOCIETY OF CHEMISTRY

www.rsc.org/advances

Colour graphic:

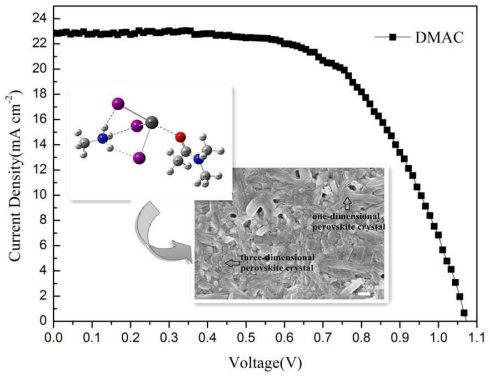

The DMAC-based deposition-crystallization method allows control over the dynamics of $CH_3NH_3PbI_3$ grain growth for the realization of high efficiency devices.

A Promising Alternative Solvent of Perovskite to Induce Rapid Crystallization for High-Efficiency Photovoltaic Devices

Minghang Lv[a], Xu Dong[a], Xiang Fang[a], Bencai Lin[a,b,c], Shuai zhang[a,b,c], Jianning Ding[*a,b,c], Ningyi Yuan[*a,b,c]

[a]Center for Low-Dimensional Materials, Micro-Nano Devices and Systems, Changzhou University, 213164, Jiangsu, China

[b]Jiangsu Collaborative Innovation Center of Photovolatic Science and Engineering, Changzhou University, 213164, Jiangsu, China

[c]Jiangsu Key Laboratory for Photovolatic Engineering and Science, Changzhou University, 213164, Jiangsu, China

* To whom correspondence should be addressed. E-mail: nyyuan@cczu.edu.cn; dingjn@cczu.edu.cn;

As solar cell structures based on planar heterojunctions have already demonstrated very impressive advances in cost-effectiveness and performance, many different solvents are being developed and gradually adopted for high-performance inorganic–organic hybrid perovskite solar cells. Here, we introduce a simple planar cell configuration with layers prepared in a fully solution-based process, in which dimethylacetamide (DMAC) serves as an effective precursor solvent that is comparable with *N*,*N*-dimethylformamide (DMF). The use of DMAC leads to a smooth and dense perovskite film via one-step deposition, whose ideal morphology enables solar cells to obtain a high power-conversion efficiency of 15.12%. We also studied the effect of different solvents through a computation of the stabilization energy between PbI_2, CH_3NH_3I, and solvent molecules. These results offer insight into the promising directions for the development of solvent engineering.

Keywords: organic–inorganic perovskite solar cells, rapid crystallization, solvent engineering, dimethylacetamide, *N*,*N*-dimethylformamide

Introduction

Organic–inorganic hybrid perovskite solar cells, the latest trend in photovoltaics, have become more popular with researchers as a result of the rapid growth in their power-conversion efficiency (*PCE*) over the past several years. Methyl ammonium lead halides such as $CH_3NH_3PbI_3$ and $CH_3NH_3PbI_xCl_{3-x}$ have been shown to be efficient light harvesters in perovskite solar cells, with a broad light absorption range in the visible to near-infrared region, high carrier mobility, and solution processability [1]. The common device architecture consists mainly of a mesopscopic and flexible structure and planar heterojunctions (PHJs) [2]. The first solid-state mesoscopic heterojunctioned perovskite solar cell was reported in 2012 and showed *PCE* of 10.9%; it comprised a mesoporous Al_2O_3 thin film whose surface was coated with a thin layer of mixed halide perovskite $CH_3NH_3PbI_2Cl$ [3]. Planar-heterojunction-structured perovskite solar cells, with the active layers deposited by the co-evaporation technique, showed a maximum *PCE* of 15.4% [4]. The planar structure is simpler and easier to control than mesostructured devices, but it is difficult to control the crystallization of perovskite and interface bonding. Zhou et al. reported a device with planar geometry and *PCE* of 19.3% by controlling the formation of the perovskite layer and optimizing interfacial structures [5], thus demonstrating that high-efficiency devices can be attained using planar structures.

With the improvement of perovskite solar cells in recent years, many methods have been developed for the deposition of perovskite films, including the solution-process, dual-source vapor deposition [6], and vapor-assisted solution process (VASP) [7]. The $CH_3NH_3PbI_3$ films associated with very impressive cell efficiencies have been prepared by these methods. There is no doubt that solution-based spin coating of the perovskite precursor is

becoming widely used in device fabrication [8], and it can be categorized as one-step deposition and two-step sequential solution deposition.

One-step deposition is a faster and simpler technique compared to those involving two steps, providing an efficient and low-cost means to produce high-performance perovskite solar cells. In previous studies, the formation of perovskite films consisted mainly of solvent vaporization, as well as perovskite crystallization and the sublimation of excess organic components [9]. In addition, different auxiliary processes and various relative rates of reactions were involved when different precursor materials and finishing conditions were used, which also had an impact on the quality of the films and crystalline morphology. Both evaporation and crystallization appear to occur simultaneously during spin coating in the conventional one-step deposition process. The main problem with spin coating, however, is that the resulting perovskite films have large island structures, many areas with uncovered pin-holes, and poor surface coverage because of the uncontrolled crystal growth of perovskite, especially on planar substrates without mesoporous scaffolds [10]. This causes some problems like light-harvesting reduction, charge recombination, film instability, and decreased device efficiency. Thus, the one-step method still needs to be improved and further optimized to reduce these disadvantages.

Much of the earlier studies on perovskite layers were focused on substrate materials, annealing temperature, heating time, spin-coating speed, and precursor concentration in one-step solution deposition. However, researchers have recently discovered that modifying the precursor solution is an efficient way to improve perovskite films and to obtain high efficiency. Carnie et al. added Al_2O_3 nanoparticles directly to the perovskite precursor solution and attained efficient lead-halide-based perovskite devices [11]. Zhao and coworkers demonstrated a novel one-step

solution approach to prepare perovskite $CH_3NH_3PbI_3$ films by adding CH_3NH_3Cl to the standard $CH_3NH_3PbI_3$ precursor solution; the results suggest that this new approach is promising for controlling $CH_3NH_3PbI_3$ growth to achieve high-performance perovskite solar cells [12]. In other words, additives can participate in the perovskite formation and play multiple roles in modulating the dynamics of perovskite crystal growth [13].

Furthermore, selecting suitable solvents of the precursor is a very critical step towards the optimization of the perovskite film's morphology. Currently, the most commonly used solvents of the perovskite precursor are *N*,*N*-dimethylformamide (DMF) and γ-butyrolactone (GBL), with the exception of dimethylsulfoxide (DMSO) and *N*-methyl-2-pyrrolidone (NMP) owing to their low volatility. The smooth surface and homogeneous crystal domains of a perovskite film can be produced by certain combinations of these solvents, such as DMF–GBL [14], GBL–DMSO [15]. There are also reports of spin coating by releasing droplets of a second solvent like chlorobenzene (CBZ) [8], toluene, and xylene to induce crystallization, or by the introduction of a simple gas-assisted method to promote evaporation of the solvent and accelerate supersaturation of the solution [16]. Extremely uniform and dense perovskite layers were formed as a result. Nevertheless, dimethylacetamide (DMAC), the homologue of DMF, had been overlooked, and it is now emerging as a promising alternative solvent of perovskite to induce rapid crystallization of perovskite films for high-efficiency photovoltaic devices.

In this study, we used DMAC as a solvent to promote rapid crystallization instead of the commonly used DMF to dissolve the precursor $CH_3NH_3PbI_3$ and deposit perovskite films by one-step deposition. This simple solution-based spin coating offers many advantages: it does not require a second solvent, additives, modification, or external assistance. Employing a DMAC solution of $CH_3NH_3PbI_3$, we also developed a strategy for obtaining a denser and

smoother perovskite film than that produced with traditional DMF. The interactions between PbI_2, CH_3NH_3I, and the solvent molecules, including DMAC and DMF, were further elucidated according to theoretical calculations, showing that DMAC has more appropriate coordinating ability than DMF. The use of DMAC dramatically improved the morphology of the perovskite films, which consisted of three-dimensional single grains and one-dimensional crystals. The resulting perovskites led to a greatly improved short-circuit current and an efficiency of 15.12% for the best-performing device with planar structure under standard reporting conditions.

Materials Preparation

All materials were purchased from either Alfa Aesar or Sigma-Aldrich. CH_3NH_3I was synthesized by reacting 27.86 ml methylamine (40% in methanol, Junsei Chemical Co.) and 30 ml hydroiodic acid (57 wt% in water, Aldrich) in a 250 ml round-bottomed flask at 0°C for 2 h with stirring. The precipitate was recovered by evaporation at 50°C for 1 h. Then, the product CH_3NH_3I, was dissolved in ethanol, recrystallized from diethyl ether, and dried at 60°C in a vacuum oven for 24 h. Spiro-MeOTAD was purchased from Aldrich.

Solar cell fabrication

Fluorine-doped transparent conducting SnO_2-coated glass substrates (FTO) were cleaned using ultrasonic washing in ethanol for 30 min and were subsequently treated in an oxygen plasma cleaning machine for 10 min. A 40-nm-thick compact layer of TiO_2 was then coated on the substrates by a spin coater at 3,000 r.p.m. for 30 s and the film was annealed at 500 °C for 60 min. The synthesized CH_3NH_3I powder was mixed with PbI_2 at a 1:1 mol ratio in DMAC or DMF at 65°C for 12 h. The concentration of $CH_3NH_3PbI_3$ was 1 mol/L. The solution was then coated onto the c-TiO_2/FTO substrate by spin-coating at 3,000 r.p.m. for 30 s, and dried

on a hot plate at 105°C for 10 min. This steps were carried out in a N_2-purged glove box (<0.1 ppm O_2 and H_2O). Subsequently, the spiro-OMeTAD-based hole-transfer layer (170 mg spiro-OMeTAD, 28.5 ul 4-tert-butylpyridine and 20 mg lithium-bis (trifluoromethanesulfonyl) imide (Li-TFSI) all dissolved in 1 ml chlorobenzene) was deposited by spin coating at 4,000 r.p.m. for 30 s. Spiro-OMeTAD stands for 2,2',7,7'-tetrakis(*N*,*N*-di-*p*-methoxyphenilamine)-9,9'-spirobifluorene. Finally, a 130 nm thick silver layer was deposited by vacuum evaporation at a pressure of 1.3×10^{-3} Pa.

Device characterization

The current-voltage (*J-V*) curves of the solar cells were measured under ambient conditions using a Keithley 2400 source meter (Keithley Instruments Inc., Cleveland,OH, USA). The cells were illuminated by a 450 W Class AAA simulator equipped with an AM1.5G filter (XES-40S1) at a calibrated intensity of 100 mW cm^{-2}, as determined by a standard silicon reference cell. The effective area of the cell was defined as 0.0405 cm^2 using a non-reflective metal mask. The crystallographic structure of the perovskite was analyzed by X-ray diffraction (XRD) (D/MAX Ultima III, Rigaku Corporation, Tokyo, Japan) using Cu Kαradi-ation. The morphology was determined by scanning electron microscopy (SEM). UV-visible (UV–vis) spectra were carried out on a Hitachi U-3010 spectrophotometer (Hitachi, Ltd., Chiyoda, Tokyo, Japan). The external quantum efficiency (*EQE*) measurements were carried out using a system consisting of a Xe lamp (300 W) with a monochromator (Oriel 74100). The light intensity was measured with an optical power meter (Ophir Optronics 70310) equipped with a calibrated thermopile head (Ophir Optronics 71964). Electrochemical

impedance spectroscopy (EIS) was conducted using a Zahner IM6ex electrochemical workstation, in which a perturbation of 10 mV was applied, and the frequency ranged from 1 Hz to 1 MHz.

Computation method

In order to investigate in depth the effect of solvents on the reaction rates of PbI_2 and CH_3NH_3I as well as the speed of crystallization of these perovskite materials, we conducted simulations of PbI_2, CH_3NH_3I, and the solvent molecules DMAC and DMF. All the calculations were performed using the GAUSSIAN-03 program. The minimum-energy structures of all molecular isomers were completely optimized using density-functional theory (DFT) employing Becke's three-parameter exchange potential and the Lee-Yang-Parr correlation functional (B3LYP). The LanL2DZ basis set was used for Pb and I atoms, whereas the 6-311++G(d,p) basis set was used for C, N, O, and H atoms. Vibrational mode analyses were systematically carried out to confirm that on a potential energy surface all the optimized geometries corresponded to a local minimum that had no imaginary frequency mode. The structural changes of the molecules under the influence of foreign water molecules were examined. To further investigate the strength of the interaction between the organic-inorganic hybrid and water molecules, a natural bonding orbital (NBO) analysis was carried out. The interaction energies were corrected for the basis set superposition error (BSSE) using the counterpoise correction method of Boys and Bernardi.20 In the NBO analysis, the stabilization energy E(2) for each donor NBO (i) and acceptor NBO (j) associated with delocalization ("2e-stabilization") i→j is estimated as:

$$E(2) = \Delta E_{ij} = q_i \frac{F(i,j)^2}{\varepsilon_i - \varepsilon_j}$$

where qi is the occupancy of the donor orbital, εi and εj are diagonal elements (orbital energies), and F(i,j) is the off-diagonal NBO Fock matrix element. Vicinal interactions between the delocalizing acceptor orbital and the orbital of the adjacent bonded atom (donor-acceptor NBOs separated by one connecting bond) can influence the molecular properties through delocalization interactions, known as the hyper conjugative effect.

Results and Discussion

Figure 1 shows the spin-coating process for the preparation of perovskite films, in a glove box, by one-step deposition on fluorine-doped tin oxide (FTO) glass substrates coated with a compact TiO_2 layer. The $CH_3NH_3PbI_3$ precursor solutions were based on the solvents DMAC and DMF. For the sample prepared from the precursor solution with DMAC as the solvent, the perovskite crystals formed immediately, and the color of the film on the substrate changed to light gray during the conventional spin-coating process. The surface appeared smooth and shiny black when heated. In contrast, for the sample prepared from the precursor solution with pure DMF as the solvent, the color change to gray was not observed during the rotations, but it continued to exhibit a rich yellow color. The films were subjected to annealing at 100 °C for 10 min to remove residual solvent and to promote crystallization. Moreover, the perovskite layer surface was rough and inhomogeneous. The above observations suggest that the DMAC solvent was the more volatile component for promoting fast nucleation and growth of crystals in the film.

Figure 2a shows XRD patterns of the two samples, with the perovskite films exhibiting almost the same crystalline phases because of the similarities between the two solvents used to prepare them. The strong diffraction peaks of (110), (220), and (310) at 2θ of 14.1°, 28.4°, and 31.81°, respectively, clearly show that both perovskite films contained the tetragonal phase. However, when XRD measurements were performed on these films later to explore their stability, different XRD patterns were obtained, as shown by a comparison of XRD spectra of DMAC- and DMF-based $CH_3NH_3PbI_3$ films that were stored in air for two days (Fig. 2b,c). For the perovskite film based on DMF, the (001) diffraction peak of PbI_2 appeared at 2θ = 12.65°, but no PbI_2 XRD signal could be detected from the perovskite films based on DMAC. In general, the presence of this characteristic diffraction peak of PbI_2

indicates degradation of the perovskite structures under humid environment (45±10% relative humidity), [17]. Our results show that the $CH_3NH_3PbI_3$ film based on the precursor dissolved in DMAC was more stable, which may have been related to the crystalline morphology of perovskite. Whether different solvents affect their stability still needs further study.

To further investigate the reasons behind the different performances of the perovskite films, scanning electron microscopy (SEM) was conducted to analyze the morphological variations driven by different solvents. Figure 3 compares the surface morphology of the DMF- and DMAC-based perovskite films. The low-magnification SEM images (Fig. 3a,c) clearly show that the DMAC-based perovskite film fully covered the surface of the FTO/glass substrate, whereas the DMF-based film with dendritic structure exhibited poor coverage on the substrate. The high-resolution SEM image (Fig. 3b) of the DMF-based perovskite film reveal that the surface exhibited a heterogeneous morphology with grain sizes in the range of 100–300 nm. In the case of the DMAC-based perovskite film, more uniform and denser crystalline perovskite domains are visible in the high-resolution SEM image (Fig. 3d), which consisted of three-dimensional single grains (100–200 nm) and one-dimensional crystals (>700 nm). This difference in morphology may have originated from the differences in the nucleation of grains and crystal growth within the films. The DMAC solution of $CH_3NH_3PbI_3$ had more supersaturation than the DMF solution of $CH_3NH_3PbI_3$, thereby promoting the rate of perovskite crystallization with more crystal nuclei. The morphologies also illustrate that a degenerative process resulted in a perovskite film that was sparser and had slower growth. Furthermore, the mixed grains with different dimensions in the DMAC-based perovskite film may have played a beneficial role in improving the carrier mobility, thus enhancing the photovoltaic properties.

Figure 4 shows UV–vis absorption spectra of perovskite films prepared from different precursor solutions. The $CH_3NH_3PbI_3$ films based on the precursor dissolved in DMAC showed strong and efficient perovskite absorption characteristics, with clear coverage at wavelengths between 350 and 650 nm. These films can lead to an improvement in device performance of perovskite solar cells [18]. In contrast, drastically decreased absorption was observed in the spectra of DMF-based films, which indicate their low nucleation rate and low surface coverage.

We fabricated $CH_3NH_3PbI_3$-based PHJ perovskite solar cells on a planar TiO_2 compact layer on FTO glass; the cells were constructed with the configuration of glass/FTO/compact TiO_2/$CH_3NH_3PbI_3$/spiro-OMeTAD/Ag, and all the film layers in the solar cells were deposited by spin coating. For comparison, two types of $CH_3NH_3PbI_3$ perovskites were prepared, one from the $CH_3NH_3PbI_3$–DMF precursor and the other from the $CH_3NH_3PbI_3$–DMAC precursor. The current-density–voltage (*J*–*V*) characteristics of the perovskite solar cells are shown in Fig. 5a. The best-performing reference device prepared from DMF showed *PCE* of 6.86% under standard AM 1.5 sunlight, with a short-circuit current density (J_{SC}) of 16.4 mA cm^{-2}, an open-circuit voltage (V_{OC}) of 0.89 V, and a filling factor (*FF*) of 0.47. The devices containing perovskite films prepared from the $CH_3NH_3PbI_3$–DMAC precursor showed significant improvements in all of the photovoltaic parameters, especially the photocurrent. It exhibited high J_{SC} of 22.8 mA cm^{-2}, V_{OC} of 1.07 V, and *FF* of 0.62, resulting in a much improved value of 15.12% for *PCE*. Our results revealed that the good photovoltaic performances of the DMAC-based PHJ devices were mainly attributable to the perovskite films deposited from the $CH_3NH_3PbI_3$–DMAC precursor solution. The uniform, dense perovskite films with grains of different dimensions resulted in improved light absorption and photoelectric property. The Fig. 5c shows the SEM cross-sectional image of a planar device developed from a DMAC solution of $CH_3NH_3PbI_3$. The

~40-nm-thick, dense TiO_2 layer acted as an electron-accepting or hole-blocking layer, the ~300-nm-thick $CH_3NH_3PbI_3$ functioned as an active optical absorption layer, and the ~200-nm-thick spiro-OMeTAD served as a hole-collecting layer. FTO glass and a ~130-nm Ag layer were used as the charge-collecting electrodes. In Fig. 5b, the reproducibility of the results is shown by a histogram of the average values of *PCE* for the perovskite solar cells. Fortunately, about 90% of the cells made from DMAC-containing precursor solution exhibited an overall efficiency of over 13.50% under standard AM 1.5 sunlight. This should be attributed to the optimized perovskite layer with uniform thickness and high crystallinity. These results are in contrast to those in a previous study, where full coverage of the perovskite film prepared from a DMF-containing precursor solution, rather than a DMAC-containing precursor solution, led to a higher device efficiency [19]. The difference in the results can be explained by the introduction of Cl^- in the earlier work [19]. Many studies have provided evidence that the charge-carrier diffusion length and lifetime of the active layer can be increased by simply introducing Cl^- into perovskite to create lattice distortions and prolong the crystal growth [20]. However, the $CH_3NH_3PbI_3$ precursor we used was a mixture of CH_3NH_3I and PbI_2, without the addition of $PbCl_2$. Our experiments indicate that it is difficult to use only DMF to control the perovskite crystallization and homogeneous nucleation. The DMAC-based deposition–crystallization method allows control of the dynamics of nucleation and grain growth of $CH_3NH_3PbI_3$, which facilitates the formation of more uniform perovskite films.

Fig. 6(a) shows the *EQE* in the range from 300 nm to 800 nm. The results suggest that the DMAC-based perovskite solar cells has a higher *EQE* value than the DMF-based perovskite solar cells in wavelength range of 350-750 nm. Therefore, the DMAC-based PHJ device has a higher J_{sc}. To further investigate the charge transfer

and recombination rates, we carried out EIS measurements on both DMAC-based and DMF-based perovskite solar cells. Nyquist plots of the devices are shown in Fig. 6(b) and (c) with the different applied bias. Two arcs of circle are observed, but no distinct transmission line (TL) behavior, which is likely due to the very thin TiO_2 films employed [21]. The inset in Fig. 6(b) and (c) is the high frequency portion and the equivalent circuit of the spectra, respectively. The series resistance (R_s) is related to the interface resistance of the FTO electrode [22]. The first semicircle at high frequency region is assigned to the recombination of the charge carriers which is modeled by a contact resistance (R_{co}) at the perovskite/HTM interface [23], while the second semicircle in the lower frequency range is associated with the recombination resistance (R_{rec}) at the TiO_2/perovskite interface. The main impedance spectra are dominated by a large semicircle [24-26]. In compare with the Nyquist plots for DMAC-based and DMF-based devices, with a forward bias of 0.55 V, the R_{co} of the two perovskite solar cells are both small, while the R_{rec} of DMAC-based perovskite solar cell is higher. With a forward bias of 0.95 V, the DMAC-based devices has a lower R_{co} and a higher R_{rec} than the DMF-based devices, indicating a lower carrier recombination rate and a higher charge transfer rate for the DMAC-based perovskite solar cell. Variation of R_{rec} with the applied bias is given in Fig. 6(d). It shows that the R_{rec} decreases for both DMAC-based and DMF-based devices with increasing bias. Moreover, it is seen that the DMAC-based perovskite solar cell displays lower recombination, seen by higher R_{rec} at comparable bias. The EIS analyses are consistent with the I-V measurements of the perovskite solar cells.

In order to investigate in detail the critical effect of solvents on the reaction rates of PbI_2 and CH_3NH_3I, as well as the crystallization of the perovskite material, we conducted simulations of the reactions. The most stable configurations of PbI_2 and CH_3NH_3I dissolved in DMF and DMAC were calculated, and the results are shown in

Fig. 7a, 7b, 7d and 7e respectively. The calculations suggest that when PbI_2 is dissolved in the solvents DMF and DMAC, Pb atoms are covalently bonded to O atoms. The bonding energy between PbI_2 and DMF is larger than that between PbI_2 and DMAC, as shown in Table 1. While CH_3NH_3I dissolves in both DMF and DMAC, it interacts with the two solvents through hydrogen bonding. Table 1 lists the stabilization energies (in kcal/mol) of the main interactions between CH_3NH_3I and DMF or DMAC: the stereoelectric interaction $n(O) \rightarrow \sigma^*_{N-H}$ (the lone pair of an O atom and the antibonding orbital of an N–H bond) and $\sigma_{O-C} \rightarrow \sigma^*_{N-H}$ (bonding orbital of an O–C bond and the antibonding orbital of an N–H bond). The interaction between CH_3NH_3I and DMAC is stronger than that between CH_3NH_3I and DMF. Figure 7c and f show clear schematic diagrams illustrating that when CH_3NH_3I and PbI_2 are dissolved in DMF (or DMAC) at the same time, CH_3NH_3I and PbI_2 can self-assemble to form the organic–inorganic hybrid structure $CH_3NH_3PbI_3$. As shown in Table 1, there are two major types of local interactions, namely, (1) $n(I) \rightarrow \sigma^*_{H-N}$ (the lone pair of an I atom and the antibonding orbital of an H–N bond) and (2) $n(O) \rightarrow \sigma^*_{Pb-I}$ (the lone pair of an O atom and the antibonding orbital of an Pb–I bond). The covalent bond between Pb and O atoms when PbI_2 is dissolved independently in the solvent is replaced by hydrogen bonds in interaction (2). Comparing the DMF- and DMAC-based situations, it can be seen that the stabilization energy of the local interaction (2) between a $CH_3NH_3PbI_3$ unit and DMAC is obviously smaller than that between a $CH_3NH_3PbI_3$ unit and DMF, which means that it is easier for the $CH_3NH_3PbI_3$ unit to escape from the solvent. Meanwhile, interaction (1) between the organic and inorganic units in $CH_3NH_3PbI_3$ is stronger in DMAC, which is favorable to crystallization of the $CH_3NH_3PbI_3$ film. Figure 7g shows the configuration of $CH_3NH_3PbI_3$ away from the solvent. As shown in Table 1, in $CH_3NH_3PbI_3$, there are two major types of local interactions; namely, (1) $n(I) \rightarrow \sigma^*_{H-N}$ (the

same as in Fig. 6c and f) and (2) n(I) → σ^*_{H-C} (the lone pair of an I atom and the antibonding orbital of an H–C bond). Figure 7h shows clear schematic diagrams illustrating that when CH_3NH_3I and $PbCl_2$ are dissolved in DMAC at the same time, CH_3NH_3I and $PbCl_2$ can also self-assemble to initially form the organic–inorganic hybrid structure $CH_3NH_3PbICl_2$. As shown in Table 1, there are three major types of local interactions, namely, (1) n(I) → σ^*_{H-N} (the lone pair of an I atom and the antibonding orbital of an H–N bond), (2) n(Cl) → σ^*_{H-N} (the lone pair of an Cl atom and the antibonding orbital of an H–N bond) and (3) n(O) → σ^*_{Pb-I} (the lone pair of an O atom and the antibonding orbital of an Pb–I bond). We can be seen that the stabilization energy of the local interaction (2) in $CH_3NH_3PbICl_2$ is stronger than corresponding interaction (1) in $CH_3NH_3PbI_3$. At the same time, interaction (3) between a $CH_3NH_3PbICl_2$ unit and DMAC is obviously smaller, which means that it is difficult to replace Cl^- with I^- in the short term and $CH_3NH_3PbICl_2$ can be left in an unusable state. Thus, the existence of $PbCl_2$ slows down the self-assemble of $CH_3NH_3PbI_3$, which hinders $CH_3NH_3PbI_3$ unit escaping from the solvent and moreover does disadvantage to the quick formation of $CH_3NH_3PbI_3$ films.

The above calculations suggest the following: DMAC is favorable for the escape of $CH_3NH_3PbI_3$ from the solvent and subsequent crystallization; PbI_2 and CH_3NH_3I diffuse easily in DMAC, and DMAC can be released quite quickly in the absence of chlorine; the in situ self-assembly of perovskite crystals between CH_3NH_3I and the PbI_2 crystal lattice would follow within a sufficient volume of space. The DMAC-based deposition–crystallization method allows control of the dynamics of nucleation and grain growth of $CH_3NH_3PbI_3$, which facilitates the formation of more uniform perovskite films. Therefore, we believe that the DMAC solution of $CH_3NH_3PbI_3$ is more specifically suited to preparing high-quality perovskite films with good coverage and homogeneity.

Conclusions

We demonstrated that DMAC is an effective solvent for controlling the dynamics of nucleation and grain growth of $CH_3NH_3PbI_3$, and it yields a smooth compact perovskite film with grains of different sizes. High-performance planar-heterojunction devices were fabricated from these high-quality perovskite thin films, which exhibited an average power-conversion efficiency of 14.23% and a best efficiency of 15.12%. On the contrary, the photovoltaic performance based on perovskite films prepared from the commonly used solvent DMF was not high owing to the poor perovskite morphology. In addition, we determined that the $CH_3NH_3PbI_3$ films based on the solvent DMAC had better visible optical absorption, carrier diffusion length, and stability in air. Furthermore, the interactions and coordination between PbI_2, CH_3NH_3I, and the solvent molecules were revealed by simulations. Based on the calculated stabilization energies together with the kinetics of $CH_3NH_3PbI_3$ crystal growth, we confirmed that the DMAC-based deposition–crystallization method enables the attainment of higher optoelectronic characteristics for perovskite films. We thus conclude that DMAC is a more suitable solvent for the preparation of the $CH_3NH_3PbI_3$ precursor solution.

Acknowledgements

This work was supported by The Privileged Development Program of Jiangsu High Education on New energy material science and engineering, the National Natural Science Foundation of china (Grant No. 51272033), the Natural Science Foundation of the Jiangsu Higher Education Institutions of China (Grant No. 14KJA430001,EEKJA48000).

References

[1] M. A. Green, A. Ho-Baillie and H. J. Snaith, *Nat. Photonics*, 2014, **8**, 506-508.

[2] H. S. Kim, S. H. Im and N. G. Park, *J. Phys. Chem. C*, 2014, **118**, 5615.

[3] M. M. Lee, J. Teuscher, T. Miyasaka, T. N. Murakami and H. J. Snaith, *Science*, 2012, **338**, 643.

[4] M. Liu, M. B. Johnston and H. J. Snaith, *Nature*, 2013, **501**, 395.

[5] H. Zhou, Q. Chen, G. Li, S. Luo, T. B. Song, H. S. Duan and Y. Yang, *Science*, 2014, **345**, 542.

[6] X. Dong, H. Hu, B. Lin, J. Ding and N. Yuan, *Chem. Commun.*, 2014, **50**, 14405.

[7] Q. Chen, H. Zhou, Z. Hong, S. Luo, H. S. Duan, H. H. Wang and Y. Yang, *J. Am. Chem. Soc.*, 2013, **136**, 622.

[8] M. Xiao, F. Huang, W. Huang, Y. Dkhissi, Y. Zhu, J. Etheridge, A. Gray-Weale, U. Bach, Y. B. Cheng and L. Spiccia, *Angew. Chem.*, 2014, **126**, 10056.

[9] A. Dualeh, N. Tétreault, T. Moehl, P. Gao, M. K. Nazeeruddin and M. Grätzel, *Adv. Funct. Mater.*, 2014, **24**, 3250.

[10] Y. Wu, A. Islam, X. Yang, C. Qin, J. Liu, K. Zhang, W. Peng and L. Han, *Energy Environ. Sci.*, 2014, **7**, 2934-2936.

[11] M. J. Carnie, C. Charbonneau, M. L. Davies, J. Troughton, T. M. Watson, K. Wojciechowski, H. Snaith and D. A. Worsley, *Chem.Commun.*, 2013, **49**, 7893.

[12] Y. Zhao and K. Zhu, *J. Phys. Chem. C*, 2014, **118**, 9412.

[13] C. C. Chueh, C. Y. Liao, F. Zuo, S. T. Williams, P. W. Liang and A. K. Y. Jen, *J. Mater. Chem. A*, 2015, DOI: 10.1039/C4TA05012F.

[14] H. B. Kim, H. Choi, J. Jeong, S. Kim, B. Walker, S. Song and J. Y. Kim, *Nanoscale*, 2014, **6**, 6679.

[15] N. J. Jeon, J. H. Noh, Y. C. Kim, W. S. Yang, S. Ryu and S. I. Seok, *Nat. materials*, 2014, **13**, 897.

[16] F. Huang, Y. Dkhissi, W. Huang, M. Xiao, I. Benesperi, S. Rubanov, Y. Zhu, X. Lin, L. Jiang, Y. Zhou, A. Gray-Weale, J. Etheridge, C. R. McNeill, R. A. Caruso, U. Bach, L. Spiccia and Y. B. Cheng, *Nano Energy*, 2014, **10**, 10-13.

[17] J. H. Kim, S. T. Williams, N. Cho, C. C. Chueh and A. K. Y. Jen, *Adv. Energy Mater.*, 2014, DOI: 10.1002/aenm.201401229.

[18] S. Y. Dou, L. T. Yan, Y. C. Liu, G. Du and P. Zhou, *J. Mater. Sci.*, 2013, **24**, 4862.

[19] D. Shen, X. Yu, X. Cai, M. Peng, Y. Ma, X. Su, L. Xiao and D. Zou, *J. Mater. Chem. A*, 2014, **2**, 20454.

[20] P. W. Liang, C. C. Chueh, X. K. Xin, F. Zuo, S. T. Williams, C. Y. Liao and A. K. Y. Jen, *Adv. Energy Mater.*, 2015, **5**, 1400960.

[21] J. A. Christians, R. C. M. Fung and P. V. Kamat, *J. Am. Chem. Soc.*, 2013, **136**, 758.

[22] G. Niu, W. Li, F. Meng, L. Wang, H. Dong and Y. Qiu, *J. Mater. Chem. A*, 2014, **2**, 705-708.

[23] M. H. Kumar, N. Yantara, S. Dharani, M. Graetzel, S. Mhaisalkar, P. P. Boix and N. Mathews, *Chem. Commun.*, 2013, **49**, 11089-11090.

[24] Y. Rong, Z. Ku, A. Mei, T. Liu, M. Xu, S. Ko, X. Li and H. Han, *J. Phys. Chem. Lett.*, 2014, **5**, 2162-2164.

[25] X. Dong, X. Fang, M. Lv, S. Zhang, J. N. Ding and N. Yuan, *J. Mater. Chem. A*, 2015, DOI: 10.1039/C4TA06128D

[26] J. Dong, Y. Zhao, J. Shi, H. Wei, J. Xiao, X. Xu, J. Luo, J. Xu, D. Li, Y. Luo and Q. Meng, *Chem. Commun.*, 2014, **50**, 13381-13383.

Figure captions

Figure 1. Schematic illustration of spin-coating process for preparing perovskite films based on a DMAC solution of $CH_3NH_3PbI_3$ (top); based on a DMF solution of $CH_3NH_3PbI_3$ (bottom).

Figure 2. X-ray diffraction spectra of as-deposited perovskite films prepared by one-step deposition of DMAC-based precursor and DMF-based precursor (a); DMF-based (b) and DMAC-based (c) perovskite films exposed in atmosphere for 2 days. The diffraction peaks for the perovskite material(circles), FTO/glass substrate (rhombuses).

Figure 3. Scanning electron microscopy images of $CH_3NH_3PbI_3$ perovskite films obtained from DMF(a,b) and DMAC(c,d) solutions.

Figure 4. UV-vis absorption spectra of $CH_3NH_3PbI_3$ perovskite layers obtained from one-step deposition of DMAC-based and DMF-based precursor.

Figure 5. (a)*J–V* curves for a PHJ solar cell (FTO/c-TiO_2/300-nm-thick perovskite layer/ Spiro-OMeTAD /Ag); (b)PCE histograms of perovskite solar cells obtained from the measurements of 25 devices; (c) Cross-sectional SEM image of PHJ solar cell containing the perovskite film prepared from the DMAC solution.

Figure 6. (a)IPCE spectra and (b,c) Nyquist plot of the DMAC-based and DMF-based perovskite solar cells; (d) variation of R_{rec} with the applied bias.

Figure 7. schematic diagram of the solute solvent interactions.

Table 1. Stabilization energy (in Kcal/mol) of main interactions between CH_3CH_3I, PbI_2, $PbCl_2$ and solvent molecule

structure	PbI_2-DMF	PbI_2-DMAC	CH_3CH_3I-DMF	CH_3CH_3I- DMAC	CH_3CH_3I-PbI_2-DMF	CH_3CH_3I-PbI_2-DMAC	CH_3CH_3I-$PbCl_2$-DMAC	$CH_3CH_3PbI_3$
Donor-Accept	Stabilization energy							
BD (O-Pb)	269.20	268.57						
$n(O)\rightarrow\sigma^*_{N-H}$			12.35	13.80				
$\sigma_{O-C}\rightarrow\sigma^*_{N-H}$			6.69	7.93				
$n(I)\rightarrow\sigma^*_{N-H}$			42.98	40.96	19.88	19.34	15.74	18.70
$n(I)\rightarrow\sigma^*_{N-H}$					9.53	9.94		18.59
$n(I)\rightarrow\sigma^*_{N-H}$					9.03	9.29		
$n(Cl)\rightarrow\sigma^*_{N-H}$							13.04	
$n(Cl)\rightarrow\sigma^*_{N-H}$							12.28	
$n(O)\rightarrow\sigma^*_{Pb-I}$					27.63	24.36	22.03	
$n(I)\rightarrow\sigma^*_{H-C}$								2.19

Fig.1

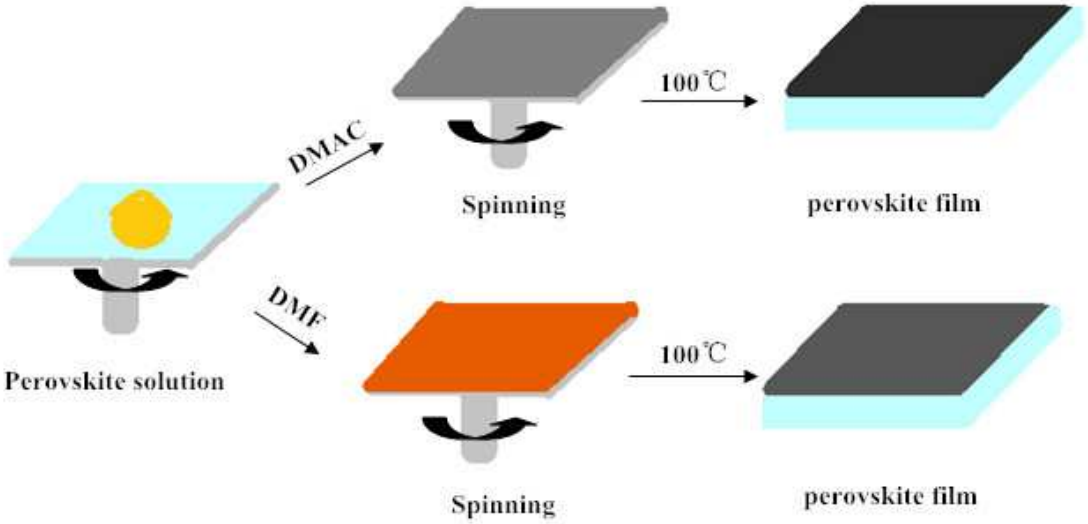

Fig.2

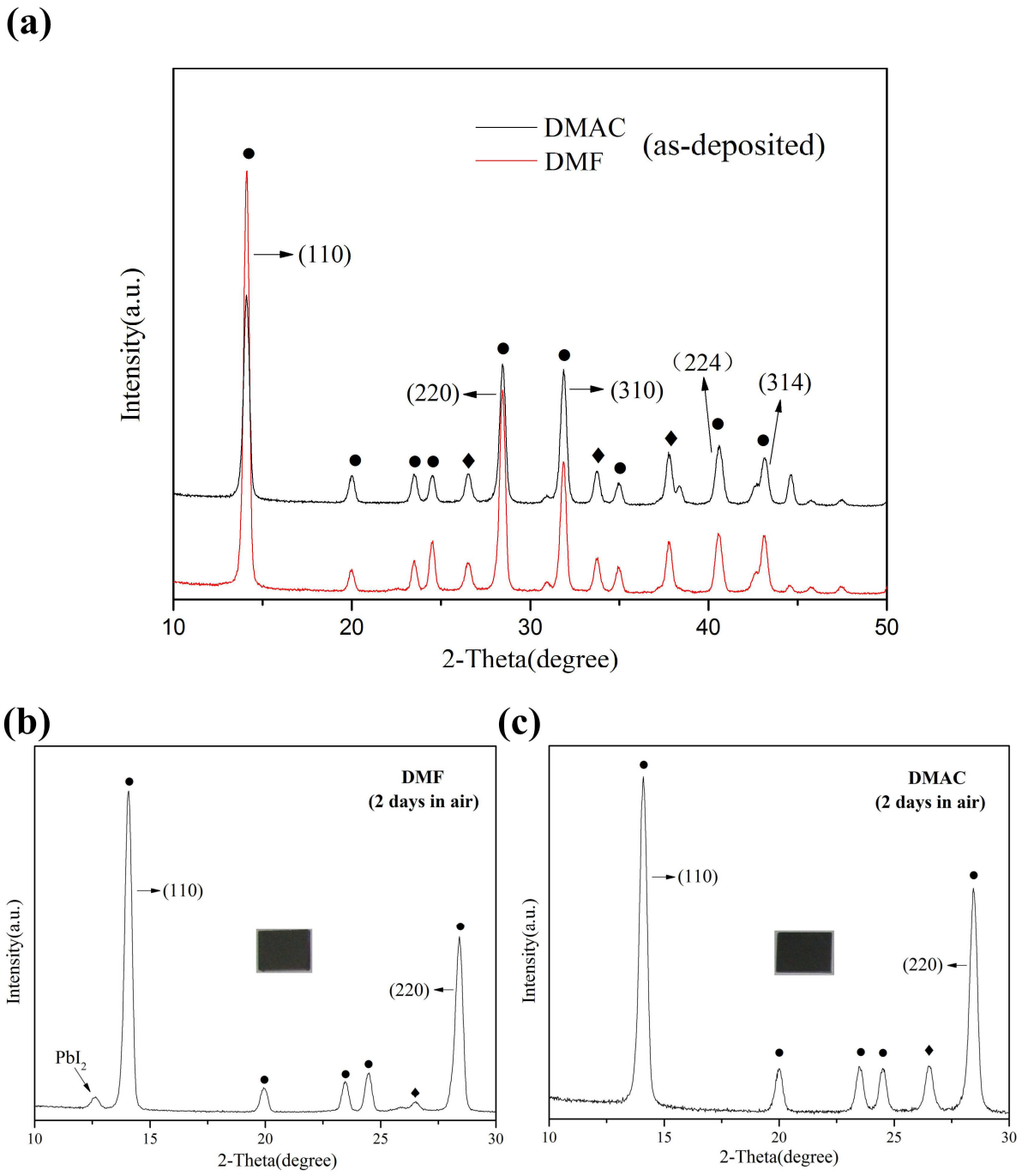

Fig.3

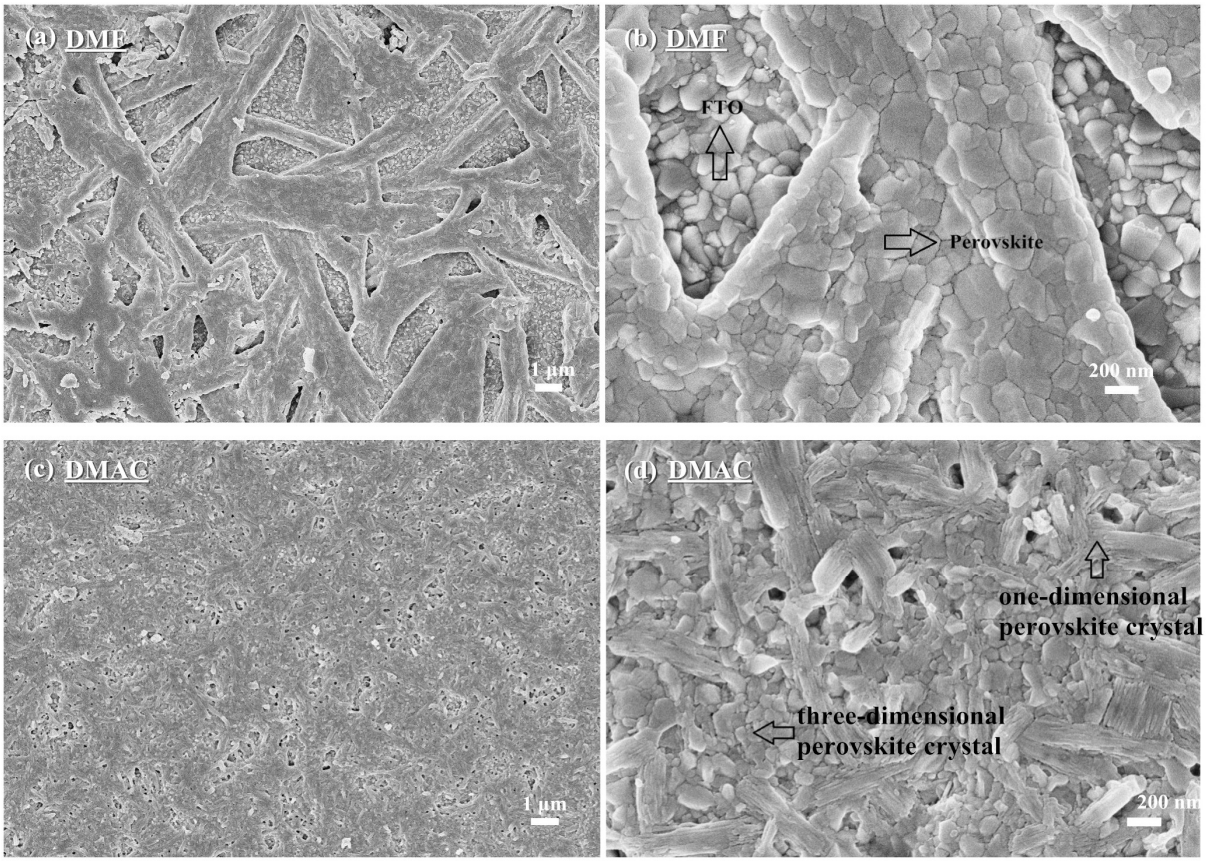

Fig.4

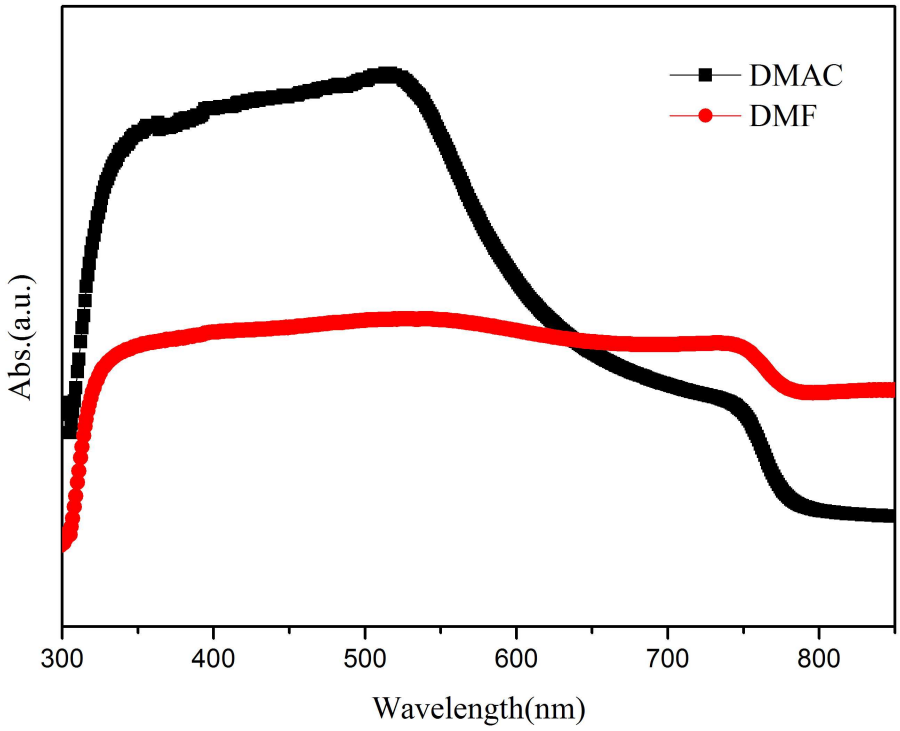

Fig.5

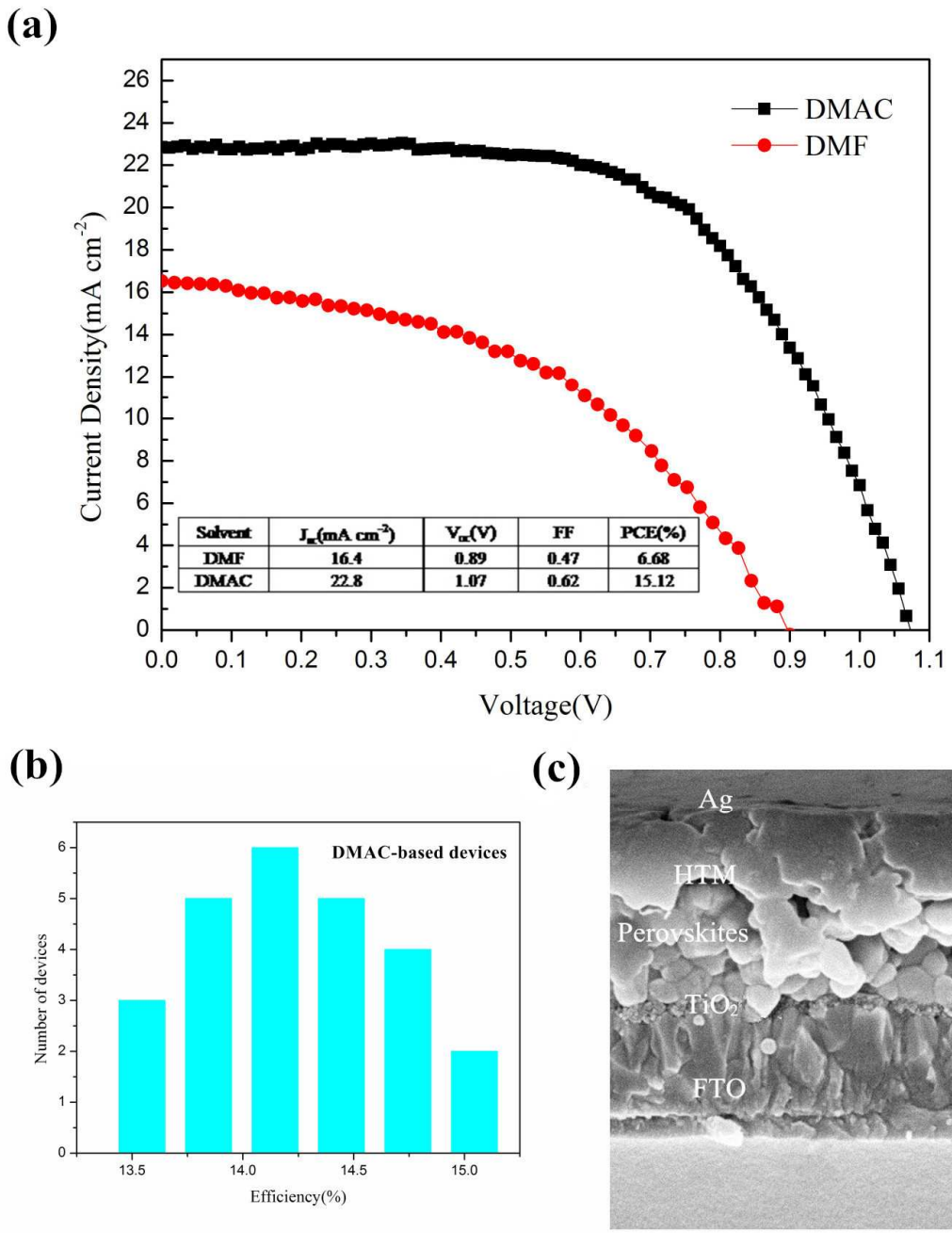

Fig.6

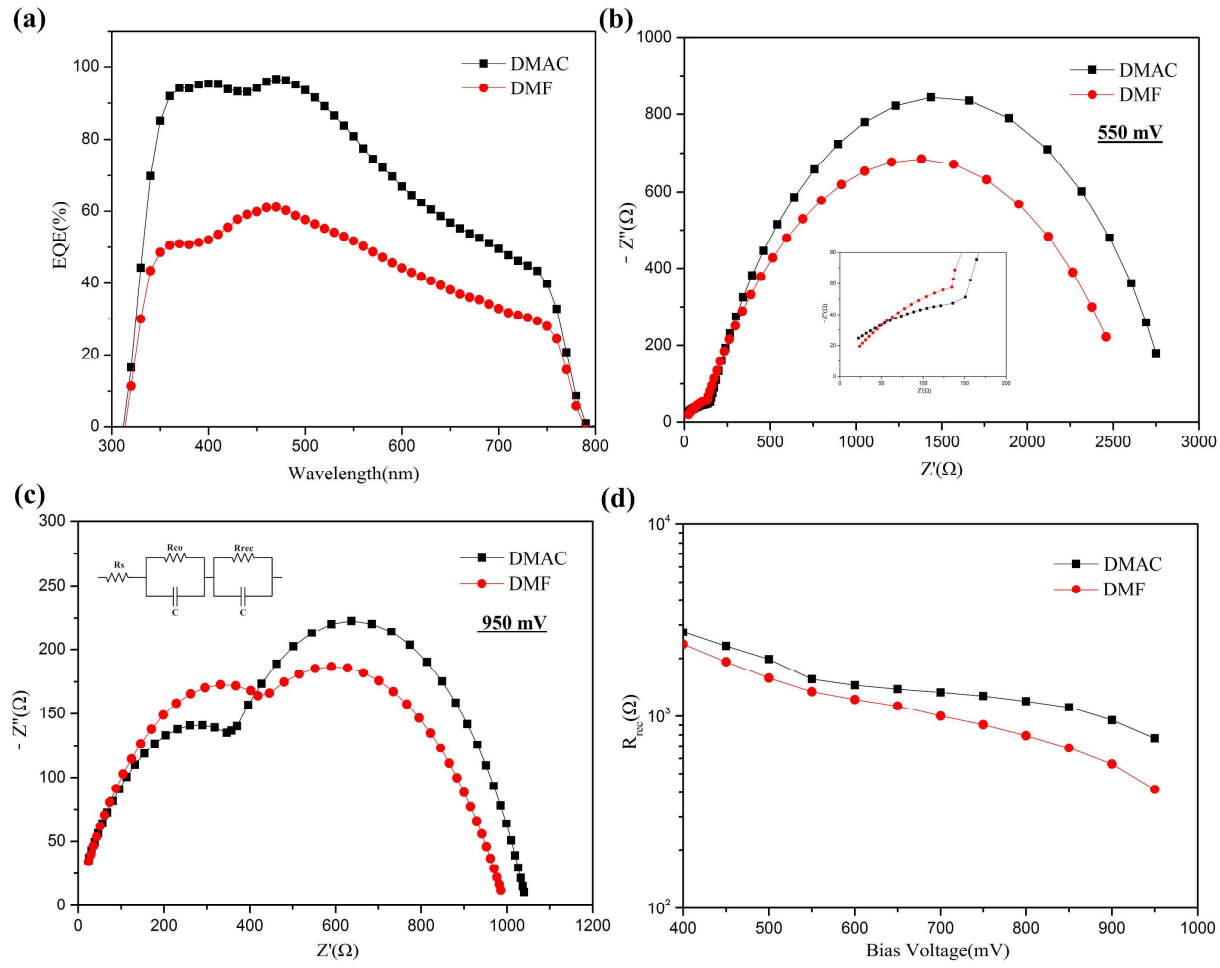

Fig.7

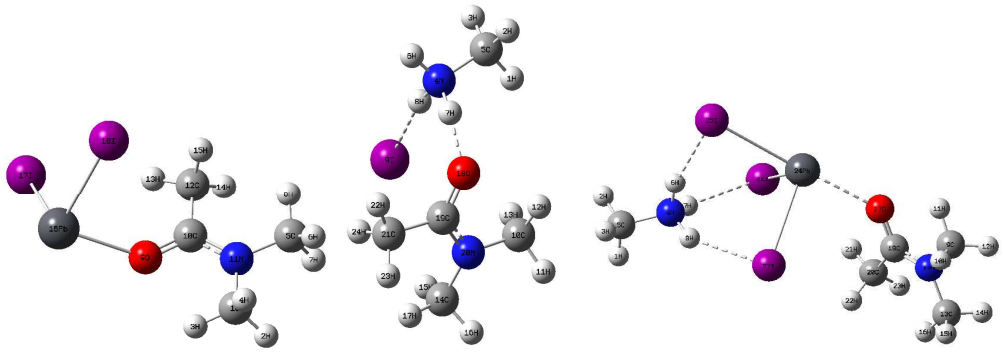

(a) PbI_2-DMAC (b) CH_3CH_3I-DMAC (c) CH_3CH_3I-PbI_2-DMAC

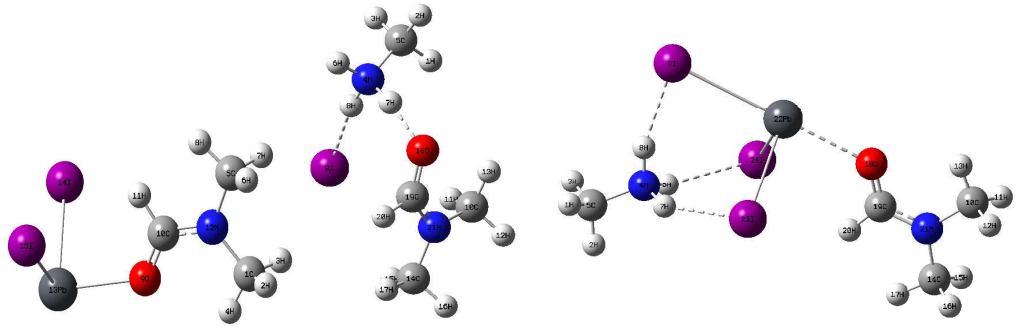

(d) PbI_2-DMF (e) CH_3CH_3I-DMF (f) CH_3CH_3I-PbI_2-DMF

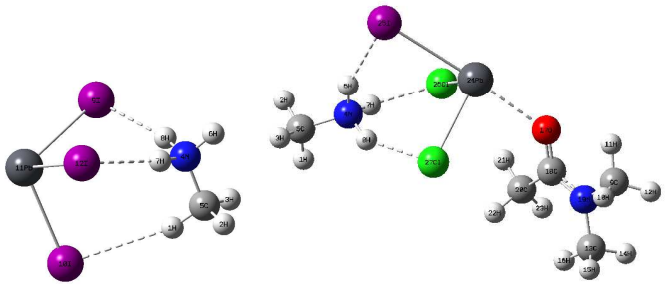

(g) $CH_3CH_3PbI_3$ (h) CH_3CH_3I-$PbCl_2$-DMAC